

Stability of Haptic Rendering: Discretization, Quantization, Time Delay, and Coulomb Effects

Nicola Diolaiti, *Student Member, IEEE*, Günter Niemeyer, *Member, IEEE*, Federico Barbagli, *Member, IEEE*, and J. Kenneth Salisbury, Jr.

Abstract—Rendering stiff virtual objects remains a core challenge in the field of haptics. A study of this problem is presented, which relates the maximum achievable object stiffness to the elements of the control loop. In particular, we examine how the sampling rate, quantization, computational delay, and amplifier dynamics interact with the inertia, natural viscous, and Coulomb damping of the haptic device. Nonlinear effects create distinct stability regions, and many common devices operate stably, yet in violation of passivity criteria. An energy-based approach provides theoretical insights, supported by simulations, experimental data, and a describing function analysis. The presented results subsume previously known stability conditions.

Index Terms—Amplifier dynamics, Coulomb friction, haptic interfaces, passivity, quantization, virtual objects.

I. INTRODUCTION

THE field of haptics aims to provide the user with a sense of touch while interacting with simulated objects in a virtual world. It uses force feedback to render the kinesthetic perception of contact with virtual objects, striving to reproduce realistic sensations.

This is commonly achieved by means of an electromechanical haptic device and associated computer interface to connect the user to the artificial world, as illustrated in Fig. 1. Impedance devices [3] apply forces computed by a virtual stiffness, which is raised as high as possible to render hard contacts. These devices exhibit low intrinsic friction and inertia to minimize dynamic distortion of the user's perception [4], and may trade off the number of actuated and sensed degrees of freedom (DOFs) to optimize performance [5].

Besides the characteristics of the mechanical device, the achievable stiffness and performance depends on the computer interface. Usually implemented as a digital control loop, this entails time discretization, quantization of both position and

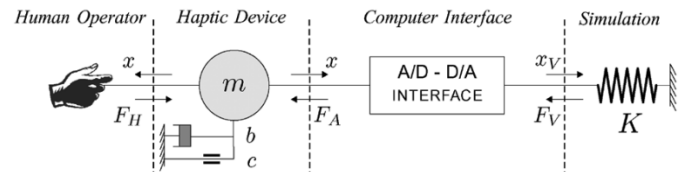


Fig. 1. Single DOF of a haptic interface rendering a virtual stiffness.

force information, computational delays, and current amplification with limited bandwidth. Clearly, these “nonidealities” limit the maximum stable feedback gain that can be reached. Implementation of stiff virtual objects has proven to be particularly demanding for common low inertia and friction devices. Yet rendering stiff objects is a basic necessity of haptic systems, and considerable research effort has been invested to analyze control strategies and increase performance.

Energy-based approaches have been used in [6]–[8] to view some of these limitations and provide stability conditions; passivity is sufficient for stability, if the operator is described by unknown passive elements [9]. The time delay introduced by the zero-order hold (ZOH) generates and injects energy into the system (*energy leaks*, according to the nomenclature used in [8]). This excess energy may cause instability if not dissipated by the haptic device's intrinsic friction or through control. For example, [10] proposes to predict the position of the device at the next time step to reduce energy leaks, while [11] dynamically estimates the energy generation and uses dissipation through a digital damper element. A port-Hamiltonian approach is followed in [12] to track and dissipate energy excess. Yet these control strategies do not explicitly account for uncertainties related to position quantization or limited actuation bandwidth. Physical friction remains a key element to dissipate energy and preserve system stability. This concept has been refined in [13] to consider computational delay, in [14] to include Coulomb friction and variable stiffness, and in [15] for quantization.

Our work analyzes how the combined effects of nonidealities limit the achievable performances, measured as the largest stable feedback gain. It shows several distinct stability regions. The haptic interface model used throughout this paper accounts for the hard nonlinearities of quantization, discretization, and delays in the controller, while considering viscous and Coulomb friction in the mechanism. In particular, Coulomb friction plays an important role in force-feedback mechanisms [16] and haptic devices.

The results are supported by a rigorous theoretical energy analysis and an approximate describing function analysis. They are validated through simulation and experiment, and are consistent with the performance of a variety of commercial haptic devices. We hope to facilitate both control and device designers alike to create effective haptic systems.

Manuscript received June 20, 2005. This paper was recommended for publication by Associate Editor W. Chung and Editor H. Arai upon evaluation of the reviewers' comments. This work was supported in part by the University of Bologna through the “Marco Polo” program, in part by the National Institutes of Health under Grant R33 LM 007295, and in part by the AGI Corporation. This paper was presented in part at the IEEE International Conference on Robotics and Automation, 2005, and in part at the IEEE World Haptics Conference, 2005.

N. Diolaiti is with DEIS, the Department of Electronics, Computer Science and Systems, University of Bologna, 40136 Bologna, Italy, and is also with the Stanford AI-Robotics Laboratory, Stanford, CA 94305 USA (e-mail: ndiolaiti@deis.unibo.it).

G. Niemeyer is with the Stanford Telerobotics Lab, Stanford University, Stanford, CA 94305 USA (e-mail: gunter.niemeyer@stanford.edu).

F. Barbagli and J. K. Salisbury are with the Stanford AI-Robotics Lab, Stanford University, Stanford, CA 94305 USA (e-mail: barbagli@robotics.stanford.edu; jks@robotics.stanford.edu).

Digital Object Identifier 10.1109/TRO.2005.862487

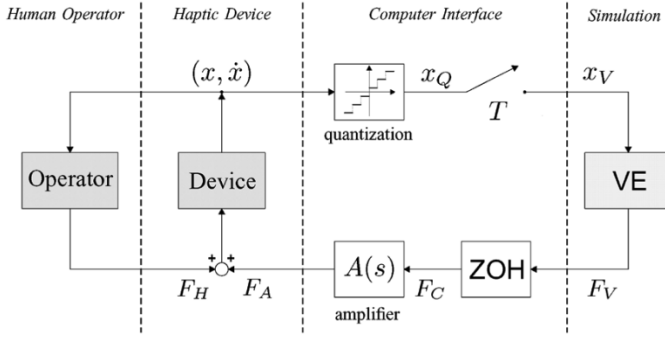


Fig. 2. Block diagram of the haptic system, connecting the human user with the virtual spring.

The paper is organized as follows. In Section II, we detail the problem and define our approach. We give and discuss the main results, including stability criteria, in Section III. They are validated through simulation in Section IV, and experimentally in Section V using a single-DOF device. The analytical proof of energy generation and dissipation is presented in Section VI, followed by the describing function analysis in Section VII. We conclude in Section VIII with some brief final remarks.

II. PROBLEM STATEMENT

A. System Description

It is a common goal in the field of haptics to render contact with a seemingly rigid virtual wall. This is generally accomplished by simulating a one-sided stiff spring force that is displayed to the user through the haptic device while the virtual contact is sustained. Our developments study the maximum achievable wall stiffness and its relation to the computer interface and device parameters. As such, we focus on a single DOF, depicted in Fig. 1. The haptic device consists of a physical inertia m and has intrinsic friction, attributed to both viscous components b and dynamic Coulomb components c . Its position x and velocity \dot{x} result from the force F_H applied by the human operator and the force F_A exerted by the amplifier to simulate the virtual stiffness K .

A computer interface relates the continuous real device to the discrete virtual world. As many researchers have recognized, the elements constituting this interface can introduce oscillatory or unstable behaviors. Shown in Fig. 2, we examine quantization of the signal, discrete sampling at time intervals T and associated ZOH, possible delays in computation of the virtual environment, and amplifier dynamics. Quantization of the command force F_C is introduced by the position sensor and the digital/analog (D/A) converter. For high stiffnesses, a single encoder tick results in a large force command corresponding to several D/A steps; in the following, we shall thus refer to the encoder resolution as the main contributor to quantization effects.

The haptic device is modeled as a point mass and described by the differential equation

$$m\ddot{x}(t) + b\dot{x}(t) + c\text{sgn}(\dot{x}(t)) = F_H(t) + F_A(t). \quad (1)$$

Meanwhile, the virtual spring force is governed by

$$F_V(hT) = -K\Delta \left(\left\lfloor \frac{x(hT)}{\Delta} \right\rfloor + \frac{1}{2} \right) \quad \forall h \in \mathbb{N} \quad (2)$$

where T is the sampling time, h denotes the discrete time variable, Δ is the combined resolution of the encoder and the D/A converter, while $\lfloor \cdot \rfloor$ refers to the integer part. Note the spring is assumed to be bidirectional, which is equivalent to the situation of a steady-state position inside the one-sided virtual wall. Without bidirectional spring forces or a bias force, contact will necessarily be broken and no further control forces will be applied. We place the origin $x = 0$ at the encoder boundary nearest the steady-state position. Furthermore, we assume a residual bias of $1/2K\Delta$ in (2), so that the spring force is symmetric about the origin but finds no steady-state value as

$$|F_V(hT)| \geq \frac{1}{2}K\Delta. \quad (3)$$

This poses the most challenging boundary conditions for the controller. The ZOH maintains this desired controller force during each servo cycle

$$F_C(t) = F_V(hT) \quad \forall t \in [hT; (h+1)T[, \quad h \in \mathbb{N}. \quad (4)$$

Finally, we consider the destabilizing lag caused by the amplifier circuitry without the benefit of the high-frequency attenuation; below its cutoff frequency ω_A , the amplifier behavior very closely matches the response of a simple delay

$$T_A = \frac{2\delta_A}{\omega_A} \quad (5)$$

where δ_A is the amplifier's damping ratio. We also allow for a computational delay T_V , typically equal to or below one sample period. This arises, for example, when complex virtual environments are simulated and necessitate collision-detection algorithms between objects. Both delays together affect the force applied to the haptic device

$$F_A(t) = F_C(t - T_D), \quad T_D = T_A + T_V \quad \forall t > 0. \quad (6)$$

B. Dimensionless Parameterization

To reduce the number of parameters, we perform a dimensional analysis. In particular, we measure position relative to a single encoder quantum Δ , time relative to the sampling interval T , and force relative to the smallest force step $K\Delta$ matching one encoder tick. Velocity is expressed relative to one encoder quantum per sampling interval Δ/T . The resulting dimensionless signals, as well as device and interface parameters, are summarized in Table I.

The differential equation (1) may be written as

$$\mu\ddot{\xi}(\tau) + \beta\dot{\xi}(\tau) + \sigma\text{sgn}(\dot{\xi}(\tau)) = \varphi_H(\tau) + \varphi_A(\tau) \quad (7)$$

where the dimensionless forces are

$$\varphi_C(\tau) = -\lfloor \xi(h) \rfloor - \frac{1}{2} \quad \forall \tau \in [h; h+1[, \quad \forall h \in \mathbb{N} \quad (8)$$

$$\varphi_A(\tau) = \varphi_C(\tau - \tau_D). \quad (9)$$

C. Stability Approach

Haptic systems are typically analyzed in the framework of passivity. Knowing that the feedback interconnection of any two passive systems is stable [17] and that most real environments

TABLE I
DIMENSIONLESS SIGNALS AND PARAMETERS

Signal / Parameter		Dimensionless Value
Spring stiffness	K	
Encoder resolution	Δ	
Sampling interval	T	
Time	t	$\tau := \frac{t}{T}$
Position	x	$\xi := \frac{x}{\Delta}$
Velocity	\dot{x}	$\dot{\xi}(\tau) = \frac{d\xi(\tau)}{d\tau} = \frac{\dot{x}T}{\Delta}$
Force	F	$\varphi := \frac{F}{K\Delta}$
Combined loop delay	T_D	$\tau_D := \frac{T_D}{T}$
Mass	m	$\mu := \frac{m}{KT^2}$
Viscous friction	b	$\beta := \frac{b}{KT}$
Coulomb friction	c	$\sigma := \frac{c}{K\Delta}$

are passive, it is a common goal to make the haptic system appear passive to the user. We follow this tradition, but we make two important notes. First, a human operator is not truly passive, and hence, the stability of a haptic interaction can not be immediately assured, even if the device appears passive. Fortunately, common experience shows that humans are skilled at interacting with passive objects and do so in a stable fashion [9]. Second, passivity of the haptic interface is not strictly necessary for stability. As we will see, the system may violate passivity requirements but result in a stable operation. As such, we carry out a Lyapunov analysis based on the energy-storage function.

More specifically, a human operator will actively move at frequencies below 10 Hz and may generate energy. But in this low-frequency band, the inertia and friction of the mechanism together with the simple virtual spring appear passive and interactions are stable. Effects of computer interface approximations and lag are negligible.

In contrast, at higher frequencies, the artificial stiffness can cause substantial problems. Instabilities usually occur at several hundred Hertz. Here the user imposes on the system an impedance, consisting of stiffness, damping, and possibly added mass. And while the impedance can change with the user's grip, it is not arbitrary; it necessarily contains relatively low stiffness and high damping. In the following, we consider the worst-case stability scenario with minimal damping, in which the user is not or is barely touching the haptic device, thus adding negligible impedance to the system. The additional damping of a stronger user grip would reinforce the natural damping of the device. As we shall see in Section III-B, such an effect enhances stability and is consistent with practical experience: a heavy grip stabilizes the interaction, while a light grip is the most challenging.

Therefore, we focus on the Lyapunov analysis of internal haptic loop connecting the virtual spring to the physical device. Using an energetic analysis, we confirm that for appropriate parameter ranges, the energy stored in the device and in the virtual spring is a suitable Lyapunov function [18].

III. MAIN RESULTS

In presenting our results, we first state the main energy-dissipation criterion and show the distinct stability regions that span the parameter space. This summarizes results of an energy-based and a describing function analysis, and is also supported by simulation and experimental work. We give the criterion in the case of no delay ($\tau_D = 0$), interpret its implications, and then provide the extension to delayed feedback.

Before proceeding, we recognize the need of a sampled data system to avoid signal aliasing. The sampling frequency ω_s must exceed twice the natural frequency ω_n

$$\omega_s = \frac{2\pi}{T} \gg 2\omega_n = 2\sqrt{\frac{K}{m}} = 2\sqrt{\frac{1}{\mu T^2}}. \quad (10)$$

This places a lower bound on the dimensionless device inertia

$$\mu \gg \frac{1}{\pi^2} \quad (11)$$

irrespective of the system behavior. In the following, we can therefore focus on the (β, σ) parameter plane, relating the dimensionless viscous and Coulomb friction to stability properties.

A. Dissipation Criterion for Zero Delay ($\tau_D = 0$)

A haptic control system depicted in Fig. 2 is proven to be energy-dissipating if

$$\left(\beta - \frac{1}{2}\right) + \frac{\sigma - \frac{1}{2}}{\dot{\xi}_{\max}} \geq 0 \quad \text{and} \quad \sigma \geq \frac{1}{2} \quad (12)$$

where a positive maximum velocity $\dot{\xi}_{\max}$ exists such that

$$|\dot{\xi}(t)| \leq \dot{\xi}_{\max} \quad \forall t \geq 0. \quad (13)$$

If the system experiences a stable interaction of the device with the virtual stiffness, the maximum velocity and energy occur at the moment of initial impact, hence

$$\dot{\xi}_{\max} = \dot{\xi}_0, \quad \text{with} \quad \xi_0 = 0. \quad (14)$$

Subsequent velocities remain bounded as the energy is dissipated. If a maximum velocity $\dot{\xi}_{\max}$ does not exist, the kinetic energy is also unbounded, and the system is clearly not energy-dissipating.

B. Stability Regions

The nonlinearities of signal quantization and Coulomb friction cause five distinct stability regions to exist within the (β, σ) parameter plane shown in Fig. 3. While the dissipation criterion (12) proves stability of regions A and E, operation in B, C, or D may generate energy. We rely on the describing function analysis, simulations, and experiments to investigate and further classify the behavior in these sections.

- [A]** $\beta > 1/2, \sigma > 1/2$: This is the only region where (12) is satisfied regardless of the maximum velocity $\dot{\xi}_{\max}$. A system operating in this region will be globally stable. Moreover, it is the only region in which the system is passive [17], [18], with Coulomb and viscous friction together dissipating any spurious energy generation due to quantization and discretization.
- [B]** $\beta > 1/2, \sigma < 1/2$: This region gives rise to small amplitude stable self-sustained oscillations (limit cycles).

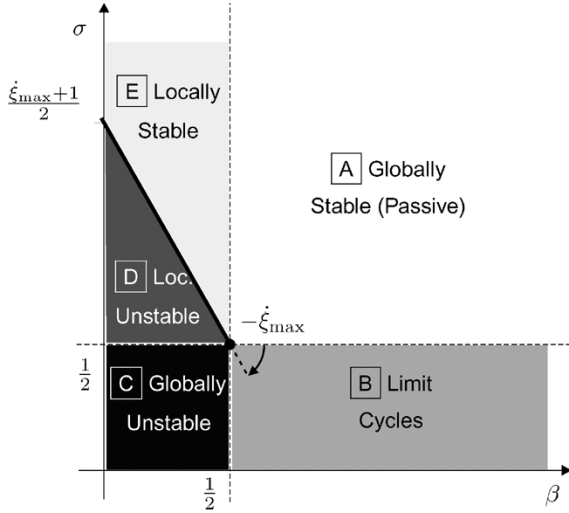


Fig. 3. Regions of the (β, σ) plane. The term “unstable” implies the system may continuously generate energy in the corresponding regions.

Analyses and tests confirm the amplitude of these limit cycles remains below a single encoder tick. Without significant Coulomb friction, the viscous damping alone is unable to suppress energy generation at these low speeds. It does, however, prevent faster motions, and hence, stabilizes the cycle.

- C** $\beta < 1/2, \sigma < 1/2$: Systems operating in this region may generate energy at all times. The describing function analysis confirms that the system is unstable and, at least under a light touch, the haptic user interaction will also be unstable.
- D** $\beta < 1/2, 1/2 < \sigma < 1/2 + \dot{\xi}_{\max}(1/2 - \beta)$: Operation below the critical line associated with (12) may again generate energy and cause instability. However, the location of the critical line is dependent on $\dot{\xi}_{\max}$ that corresponds to the initial velocity (14). The instability is therefore dependent on initial conditions and marked as local.
- E** $\beta < 1/2, \sigma > 1/2 + \dot{\xi}_{\max}(1/2 - \beta)$: If the device velocity remains limited below the threshold $\dot{\xi}_{\max}$, Coulomb friction is efficient in dissipating energy even if $\beta < 1/2$. Energy in this region is monotonically decreasing. Analogously to region D, the boundary depends on initial conditions through $\dot{\xi}_{\max}$ and stability is again local.

We find that most haptic devices rendering their maximum stable stiffness operate in region E. Their dissipation is dominated entirely by Coulomb friction, which works well at low speeds. Should these systems experience a velocity faster than the maximum velocity allowed by device friction and control loop parameters

$$\dot{\xi}_{\max} = \frac{\sigma - 1/2}{1/2 - \beta} \Leftrightarrow \dot{x}_{\max} = \frac{2c - K\Delta}{KT - 2b} \quad (15)$$

they would become unstable. At such high velocities, Coulomb friction provides little effective dissipation, compared with viscosity. As users can in practice achieve only limited velocities,

they will not distinguish operations in regions A and E, where the total energy monotonically decreases.

Table II summarizes the relevant data, expressed in Cartesian space, for a common set of commercially available haptic devices. The dimensionless parameters clearly show operation in the locally stable region E, also depicted in Fig. 4. We investigated the Omega and Delta from Force Dimension, the Impulse Engine 2000 force-feedback joystick from Immersion, the MIT Toolhandle [19], the Phantom 1.0 [4] from Sensable, and the MPB Freedom6. Manufacturer specifications and identification procedures analogous to [20] provide estimates of mass and friction coefficients. Also given are the encoder resolution, typical sampling intervals, and maximum achievable stiffness that can be rendered oscillation-free without additional human stabilization. Note that except for the Impulse Engine, the viscous friction coefficients could only be bounded due to the resolution of the measurement instruments and estimation techniques.

Finally, for comparison only, we show the lumped parameters of a human operator in a configuration typical of haptic interaction [21]. Note especially the high viscous damping. As the human stiffness and damping apply in parallel with the device parameters, the effective viscous coefficient is substantially raised by appropriate human touch; i.e., users may shift the system from region E into the passive region A. This reiterates and supports our discussion of Section II-C and our choice to focus the stability analysis on the worst-case scenario with no user dissipation.

C. Interpretation

The stability regions may be seen as generalizing Colgate’s inequality ($\beta > 1/2$ in the dimensionless formulation) [7] to include dynamic Coulomb friction and sensor quantization. If the system is sampled without quantization, the dissipation criterion (12) relaxes to

$$\left(\beta - \frac{1}{2}\right) + \frac{\sigma}{\dot{\xi}_{\max}} \geq 0 \Leftrightarrow \left(b - \frac{KT}{2}\right) + \frac{c}{\dot{x}_{\max}} \geq 0 \quad (16)$$

and regions B and C are removed from the parameter plane. We find Coulomb friction assisting viscous damping, especially for small velocities, consistent with physical intuition.

We also see qualitative distinctions between the two dissipation effects. From (12), the viscous friction

$$\beta \geq \frac{1}{2} \Leftrightarrow b \geq \frac{KT}{2} \quad (17)$$

should balance the stiffness and effective delay due to the sampling and ZOH; the phase lag of the ZOH is compensated by the phase lead of the viscosity. Coulomb friction

$$\sigma \geq \frac{1}{2} \Leftrightarrow c \geq \frac{K\Delta}{2} \quad (18)$$

must be able to hold the device against the step force changes due to quantization to avoid limit cycles. Both effects together support passive operation; one effect by itself can only create a locally stable system or stable limit cycles.

For a particular device, with fixed mass m , viscosity b , and Coulomb friction c , we may influence stability by selection of K, T , and Δ . Increasing stiffness K affects both β and σ ; the operation point moves in a straight line toward the origin and

TABLE II
PARAMETERS OF COMMON DEVICES

Device	m [Kg]	b [Ns/m]	c [N]	Δ [μ m]	T [ms]	K [N/m]	μ	β	σ
Delta	0.250	0.01	0.883	30	0.33	14500	155.2	0.002	2.03
Freedom 6	0.250	0.01	0.06	20	1	2400	104.2	0.025	1.25
Impulse Engine	0.032	0.02	0.024	31.4	0.2	800	1007.8	0.13	0.97
MIT Toolhandle	0.119	0.001	0.034	20.1	1	3125	38.19	0.0003	0.54
Omega	0.220	0.01	0.147	10	0.33	14500	136.6	0.002	1.01
Phantom 1.0	0.072	0.005	0.038	29.1	1	1015	70.55	0.004	1.29
Human Operator	0.150	4.8				600			

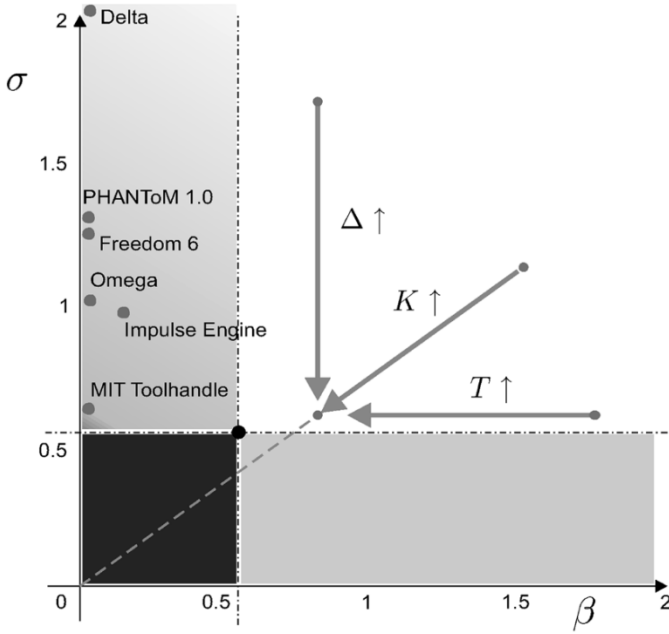


Fig. 4. Effects of wall stiffness K , sampling time T , and encoder resolution Δ on the (β, σ) plane.

hence toward instability, as shown in Fig. 4. Consistent with intuition, larger sampling times T and encoder steps Δ are also destabilizing, lowering β or σ , respectively.

D. Extension To Delayed Feedback

Most practical systems experience some amplifier and computational delay in addition to the effective delay of the ZOH. A haptic control system with delay τ_D is proven to be energy-dissipating if

$$\sigma - \frac{1}{2} - \ddot{\xi}_{\max} (\tau_D^2 + \tau_D) + \dot{\xi}_{\max} \left(\beta - \frac{1}{2} - \tau_D \right) \geq 0 \quad (19)$$

where a positive maximum velocity $\dot{\xi}_{\max}$ and a positive maximum acceleration $\ddot{\xi}_{\max}$ exist such that

$$|\dot{\xi}(t)| \leq \dot{\xi}_{\max} \quad |\ddot{\xi}(t)| \leq \ddot{\xi}_{\max} \quad \forall t \geq 0. \quad (20)$$

The delay raises the values of β and σ required for stable operation. It also splits the former passive region A into two sections F1 and F2. In F2, the system may briefly generate energy. However, unlike its neighbor B, extended motions in F2 dissipate energy and the system remains stable. This is confirmed by

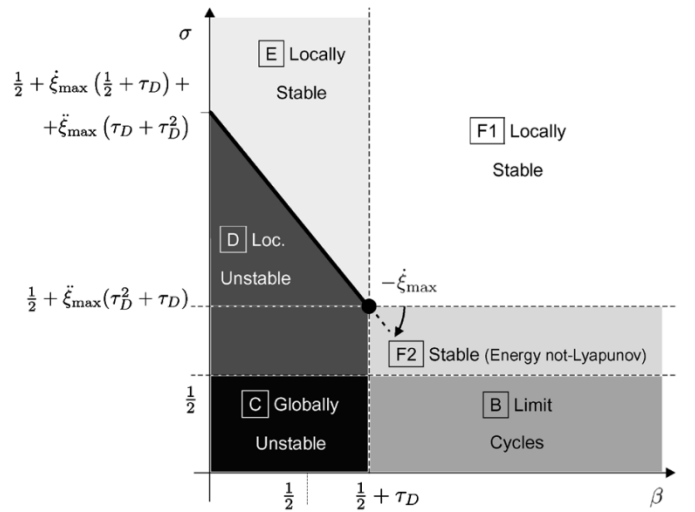


Fig. 5. Regions of the (β, σ) plane for delayed feedback. The term “unstable” again implies the system may continuously generate energy.

the describing function analysis and is labeled as stable, but remarking that the total energy here is not a Lyapunov function.

In region F1, energy dissipation is continual and the system is thus stable, with the energy monotonically decreasing. To label this area as passive, we would have to postulate a global maximum acceleration valid for all signals or initial conditions. In practice, this may occur with amplifier saturation, but falls beyond the assumptions we wish to make here.

Finally, we note these results are consistent with [14]. Under the assumptions of $\ddot{\xi}_{\max} = \sigma/(\beta\tau_D)$, $\tau_D = 1$, and without quantization, Mahvash and Hayward determine the stability criterion $\beta \geq 2$.

IV. SIMULATIONS

Before providing an analytic proof of the mappings (12) and (19), we confirm the stability regions illustrated in Figs. 3 and 5 through simulations.

The dimensionless model (7) has been simulated assuming no initial deflection $\xi_0 = 0$, different initial velocities $\dot{\xi}_0$, and a null input from the human operator.

A grid of 714 different values of (β, σ) has been considered. The state vector $(\xi, \dot{\xi})$ has been evaluated at $\tau = 5 \times 10^4$, corresponding to $t = 50$ s for a sampling time $T = 1$ ms, to determine the stability of each operating point. Zero crossing detection allowed increased resolution of the numerical solver and accurate

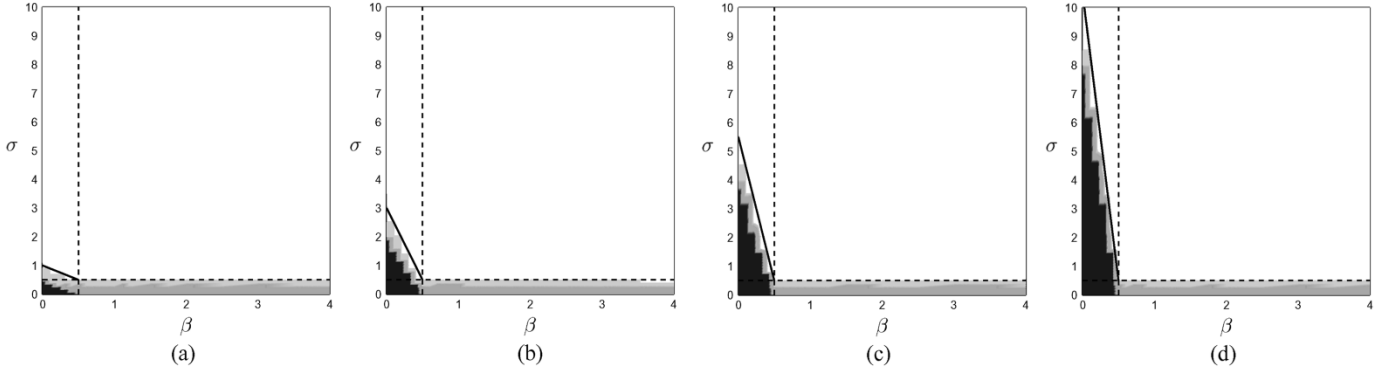


Fig. 6. Stability regions on the (β, σ) plane for $\tau_D = 0$ and $\mu = 100$. Dark, medium, light, and white areas represent growing, persistent, nonmonotonically decaying, and monotonically vanishing energy and oscillations. (a) $\dot{\xi}_{\max} = \dot{\xi}_0 = 1$. (b) $\dot{\xi}_{\max} = \dot{\xi}_0 = 5$. (c) $\dot{\xi}_{\max} = \dot{\xi}_0 = 10$. (d) $\dot{\xi}_{\max} = \dot{\xi}_0 = 20$.

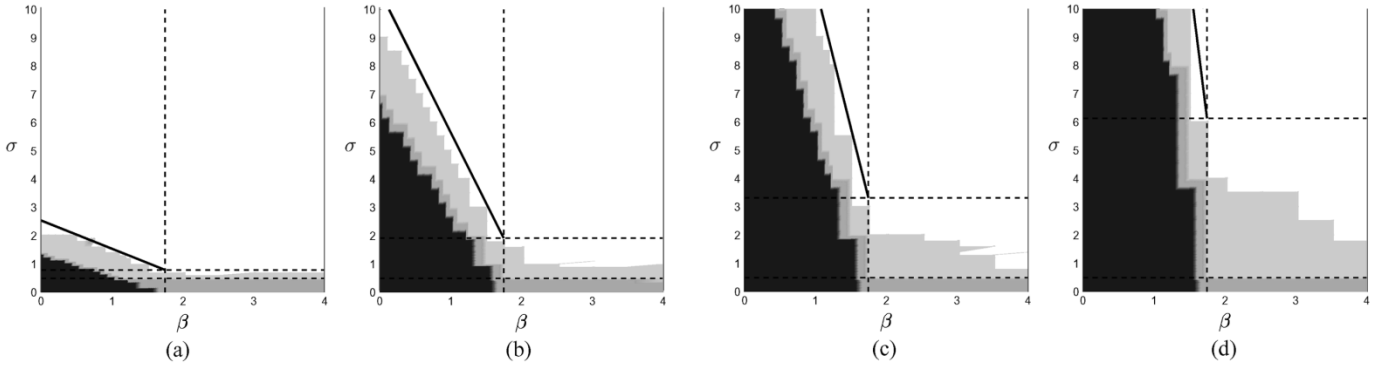


Fig. 7. Stability regions on the (β, σ) plane for $\tau_D = 1.25$ and $\mu = 100$. (a) $\dot{\xi}_{\max} = \dot{\xi}_0 = 1$. (b) $\dot{\xi}_{\max} = \dot{\xi}_0 = 5$. (c) $\dot{\xi}_{\max} = \dot{\xi}_0 = 10$. (d) $\dot{\xi}_{\max} = \dot{\xi}_0 = 20$.

simulation of quantization and Coulomb friction. High numerical resolution about the equilibrium allowed also discrimination of oscillating and converging trajectories.

Results obtained with $\mu = 100$ and four different initial velocities, for a system without time delays, are shown in Fig. 6. The dark areas represent growing oscillations, medium areas denote persistent oscillations, light and white areas show vanishing oscillations with nonmonotonically and monotonically decaying energy, respectively.

We see a good correspondence between the prediction and simulation outcomes with strong agreement with the stability regions of Fig. 3. We note that (12) stems from a worst-case analysis, so that the actual stability regions are slightly larger than predicted.

The same simulations have been repeated with a time delay $\tau_D = 1.25$, and the results are shown in Fig. 7. We again find good correspondence to the regions of Fig. 5, and, in particular, notice the shifted borders due to the delay.

V. EXPERIMENTAL RESULTS

Experimental validation of the analytical results has been carried out by means of a Maxon RE35 motor equipped with an encoder having 8192 counts per revolution. As a rotational device, positions and forces in (1) correspond to angles and torques. The current amplifier, a Copley model 403, was commanded via a 14-bit D/A interface from the **RTAI-Linux** control loop. The amplifier was configured to have a bandwidth of 3 kHz with servo rates varying from 100 Hz to 1 kHz. Coulomb friction was estimated at $c = 2 \times 10^{-3}$ Nm, substantially higher than

viscous friction $b = 9 \times 10^{-6}$ Nm/rad s; the motor inertia was $m = 6.28 \times 10^{-6}$ Kg m². Variations of β and σ were obtained by artificially reducing the servo rate and encoder resolution.

Because of the simplicity of the virtual environment, the computational delay was negligible. Similarly, due to the configuration, the time delay related to the amplifier dynamics was also negligible. We therefore compare the experiments against criterion (12) and Fig. 3.

In contrast to the simulations, an initial deflection ξ_0 with no motion ($\dot{\xi}_0 = 0$) was used to create repeatable conditions. An equivalent maximum velocity $\dot{\xi}_{\max}$, to separate regions of the (β, σ) plane, was computed as if all potential energy was transferred to kinetic energy.

Fig. 8 shows the outcomes obtained in different regions of the (β, σ) plane. The left portion of each graph shows the operating point and the critical line associated with the initial condition, while the right side shows the temporal diagram of the angular displacement. In the right diagram, the dashed horizontal lines correspond to ± 1 encoder tick. In Fig. 8(a), we evaluated a point located in the globally stable region and, despite the high initial velocity seen by the steep slope of the critical line, the position converges to the origin. By artificially lowering the encoder resolution, the operating point is moved to region B. In Fig. 8(b), we see, as predicted, persistent oscillations below a single encoder tick. Finally, by changing the servo rate, operations in the locally stable and unstable regions D-E were tested. Variation in the initial conditions changes the critical boundary line to below [Fig. 8(c)] and above [Fig. 8(d)] the operating point. As predicted, with increased initial energy in the virtual spring, the system becomes unstable.

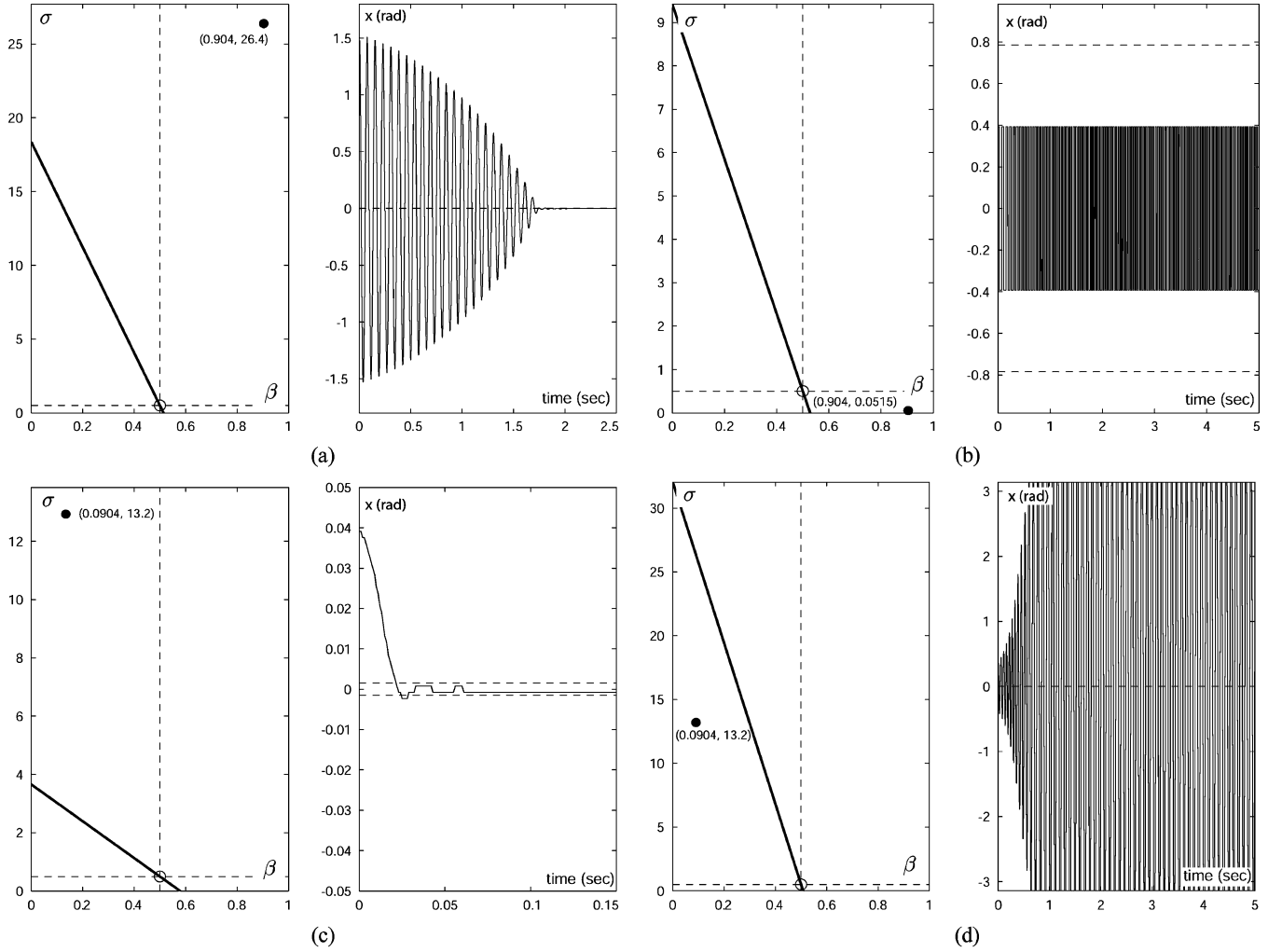


Fig. 8. Characteristic points and critical line representing initial velocity on the (β, σ) plane (left diagrams). The resulting behavior $x(t)$ is plotted on the right diagram. (a) Globally stable. (b) Limit cycle. (c) Locally stable. (d) Locally unstable.

VI. ENERGETIC ANALYSIS OF DIGITAL SPRINGS

From an informal point of view, the system of Fig. 2, comprising the device, the computer interface, and the virtual environment, is passive if only the stored energy can be extracted by the user.

However, previous work [6]–[8] showed energy generation for a discrete time, nonquantized virtual spring due to the time delays introduced by the discrete time implementation.

The causes of nonpassive behaviors can be easily analyzed by means of the displacement/force diagrams shown in Fig. 9. We compare a physical spring φ_P , a quantized *but time-continuous* spring φ_Q , a discretized *but nonquantized* spring φ_Z , and the digital (i.e., quantized and discretized) counterpart φ_C seen in the haptic system (8)

$$\varphi_P(\tau) = -\xi(\tau) \quad (21)$$

$$\varphi_Q(\tau) = -[\xi(\tau)] - \frac{1}{2} \quad (22)$$

$$\varphi_Z(\tau) = -\xi(h) \quad \forall \tau \in [h; h+1[\quad (23)$$

$$\varphi_C(\tau) = -[\xi(h)] - \frac{1}{2} \quad \forall \tau \in [h; h+1[. \quad (24)$$

The compression ($\dot{\xi} > 0$) and the restitution ($\dot{\xi} < 0$) phases of a linear physical spring generate exactly overlapping curves

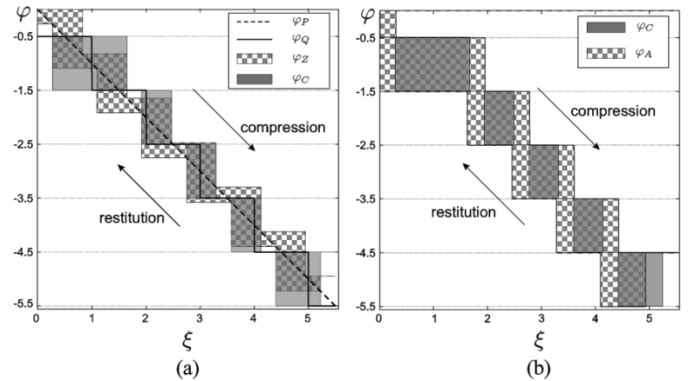


Fig. 9. Comparison of force/displacement diagrams. Left: physical (dashed), quantized (solid), time discrete (square filling), and digital (gray filled) spring. Right: Digital (gray filling) and digital delayed spring (square filling).

[dashed line in Fig. 9(a)], energy supplied during compression is entirely extracted during restitution. In other words, energy is not dissipated nor generated. The corresponding diagram for φ_Q is given by the solid line of Fig. 9(a). Though no longer smooth, the compression and restitution forces still match, and again, no energy is generated nor dissipated. Quantization is purely position-dependent, and by itself is not a source of energy leaks.

On the other hand, time discretization causes **hysteresis loops** to arise. The net result of the compression and the restitution phase is work that the haptic display does on the human operator and corresponds to generated energy. The square filled and the gray filled diagrams of Fig. 9(a) represent the behavior of φ_Z and of its digital counterpart φ_C , respectively. Comparing the generated energies, we note that the latter can be either larger (see Fig. 9(a) at $\xi \simeq 1$) or smaller (see $\xi \simeq 2$) than the former. The loss of information related to the quantization process affects the overall energy balance. A worst-case analysis is required to estimate the maximum amount of additional energy generated because of the combined effect of quantization and sampling.

Finally, the digital spring φ_C is compared with its delayed version φ_A (9). When $\tau_D > 0$, a larger amount of energy is likely to be generated. However, situations may arise (see Fig. 9(b) at $\xi \simeq 5$) when the delayed spring φ_A generates less energy. Again, a worst-case analysis is necessary to account for the delay τ_D .

In order to formalize these behaviors, (22) and (7) can be used to obtain

$$\varphi_H(\tau) = [\mu\ddot{\xi}(\tau) - \varphi_Q(\tau)] + [\beta\dot{\xi}(\tau) + \sigma\text{sgn}\dot{\xi}(\tau)] - [\varphi_A(\tau) - \varphi_Q(\tau)]. \quad (25)$$

With $\varphi_H(\tau)\dot{\xi}(\tau)$ describing the instantaneous dimensionless power delivered by the operator to the haptic system, the energy exchange during a generic time interval $[\tau_0, \tau_1]$ is

$$\int_{\tau_0}^{\tau_1} \varphi_H(\tau)\dot{\xi}(\tau) d\tau = \mathcal{H}_T(\tau_1) - \mathcal{H}_T(\tau_0) + E_d(\tau_0, \tau_1) - E_g(\tau_0, \tau_1) \quad (26)$$

where the following definitions have been used:

$$\mathcal{H}_T(\tau_1) - \mathcal{H}_T(\tau_0) := \int_{\tau_0}^{\tau_1} [\mu\ddot{\xi}(\tau) - \varphi_Q(\tau)]\dot{\xi}(\tau) d\tau \quad (27)$$

$$E_d(\tau_0, \tau_1) := \int_{\tau_0}^{\tau_1} [\beta\dot{\xi}(\tau) + \sigma\text{sgn}\dot{\xi}(\tau)]\dot{\xi}(\tau) d\tau \quad (28)$$

$$E_g(\tau_0, \tau_1) := \int_{\tau_0}^{\tau_1} [\varphi_A(\tau) - \varphi_Q(\tau)]\dot{\xi}(\tau) d\tau. \quad (29)$$

Here $\mathcal{H}_T(\tau) = \mathcal{H}_T(\xi(\tau), \dot{\xi}(\tau))$ is a positive definite function representing the energy stored by the haptic interface, E_d represents the energy dissipated because of physical friction, while E_g is the energy generated by the “nonidealities” in the control loop.

By recalling the notion of dissipativity [17], [18], system (7) connecting φ_H to $\dot{\xi}$ is passive if

$$E_d(\tau_0, \tau_1) \geq E_g(\tau_0, \tau_1) \quad \forall \tau_1 \geq \tau_0 \quad (30)$$

for any initial conditions and user inputs. Then physical friction overcomes any spurious energy generation. Following arguments of Section II-C, we focus on the stability of the haptic system without user inputs. If the system is passive, \mathcal{H}_T always monotonically vanishes and can serve as a Lyapunov function to verify global stability. In this setting, we further recognize that depending on system parameters, (30) may hold only for a limited set of initial conditions. This behavior is characteristic of local stability.

In the following, the analytic expression of \mathcal{H}_T will be computed and (30) will be investigated, considering first the non-delayed case $\tau_D = 0$, and then generalizing the result to $\tau_D > 0$.

A. Storage Function of A Quantized Spring

The total energy $\mathcal{H}_T(\xi, \dot{\xi})$ of the haptic display is given by the sum of the kinetic energy of the device $\mathcal{H}_k = (1/2)\mu\dot{\xi}^2$ and of the pseudoelastic potential energy $\mathcal{H}_e(\xi)$ stored by the quantized, time-continuous spring φ_Q

$$\mathcal{H}_e(\xi) = - \int \varphi_Q(\tau)\dot{\xi}(\tau) d\tau = - \int \varphi_Q(\xi) d\xi. \quad (31)$$

To compute $\mathcal{H}_e(\xi)$, we define the quantization error as

$$\rho = \xi - \lfloor \xi \rfloor \quad 0 \leq \rho < 1 \quad (32)$$

which is a function exclusively of the position ξ . Its integral is given by

$$\int_0^\xi \rho(\chi) d\chi = \frac{1}{2}\lfloor \xi \rfloor + \frac{1}{2}\rho^2(\xi). \quad (33)$$

From (22), the potential energy may be computed as

$$\mathcal{H}_e(\xi) = \int_0^\xi \left(\chi - \rho(\chi) + \frac{1}{2} \right) d\chi = \frac{1}{2}\xi^2 + \frac{1}{2}(\rho(\xi) - \rho^2(\xi)) \quad (34)$$

where the term depending on $\rho(\xi)$ is always positive, because $\rho \in [0; 1[$. Finally, $\mathcal{H}_T(\xi, \dot{\xi})$ is given by

$$\mathcal{H}_T(\xi, \dot{\xi}) = \frac{1}{2}\mu\dot{\xi}^2 + \frac{1}{2}\xi^2 + \frac{1}{2}(\rho(\xi) - \rho^2(\xi)). \quad (35)$$

B. Energy Dissipation

We consider viscous and dynamic Coulomb friction, represented by the dimensionless parameters β and σ , and provide a lower bound for their energy dissipation. Coulomb friction is most effective at low velocity, while viscosity dominates at high speed. We ignore any additional frictional phenomena that would further increase the dissipation. By recalling (28), the dissipated energy in the time interval $\tau \in [\tau_0; \tau_1]$ is expressed by

$$E_d(\tau_0, \tau_1) = \int_{\tau_0}^{\tau_1} \beta\dot{\xi}^2(\tau) d\tau + \int_{\tau_0}^{\tau_1} \sigma|\dot{\xi}(\tau)| d\tau = E_\beta(\tau_0, \tau_1) + E_\sigma(\tau_0, \tau_1). \quad (36)$$

A lower bound for E_β , representing dissipation due to viscous friction, can be obtained from the Cauchy–Schwarz inequality

$$\left(\int_{\tau_0}^{\tau_1} \dot{\xi}^2(\tau) d\tau \right)^{\frac{1}{2}} \left(\int_{\tau_0}^{\tau_1} 1^2 d\tau \right)^{\frac{1}{2}} \geq \left| \int_{\tau_0}^{\tau_1} 1\dot{\xi}(\tau) d\tau \right| \quad (37)$$

which leads to

$$E_\beta(\tau_0, \tau_1) \geq \beta \frac{(\xi(\tau_1) - \xi(\tau_0))^2}{\tau_1 - \tau_0}. \quad (38)$$

The triangle inequality may be used to bound the dissipation E_σ due to the dynamic Coulomb friction

$$\int_{\tau_0}^{\tau_1} |\dot{\xi}(\tau)| d\tau \geq \left| \int_{\tau_0}^{\tau_1} \dot{\xi}(\tau) d\tau \right| = |\xi(\tau_1) - \xi(\tau_0)|. \quad (39)$$

Thus, the total dissipated energy E_d is lower bounded by

$$E_d(\tau_0, \tau_1) \geq \beta \frac{(\xi(\tau_1) - \xi(\tau_0))^2}{\tau_1 - \tau_0} + \sigma|\xi(\tau_1) - \xi(\tau_0)|. \quad (40)$$

In other words, friction losses are minimized when the device moves from $\xi(\tau_0)$ to $\xi(\tau_1)$ with constant velocity.

C. Energy Generation and Balance for $\tau_D = 0$

In parallel to Section III, we first analyze energy generation in the case $\tau_D = 0$. In this situation, we have $\varphi_A(t) = \varphi_C(t)$, and E_g in the time interval $\tau \in [\tau_0; \tau_1[$ becomes

$$E_g(\tau_0, \tau_1) = \int_{\tau_0}^{\tau_1} [\varphi_C(\tau) - \varphi_Q(\tau)] \dot{\xi}(\tau) d\tau. \quad (41)$$

To simplify the analysis, we place the initial time $\tau_0 = h$ at the beginning of a sampling interval. The dissipation inequality (30) must hold for any time $\tau_1 \geq \tau_0$, which can span multiple sampling periods. This is assured if energy generation is balanced by dissipation during each sampling period or fraction thereof. And so, we examine the generation between h and $\tau_1 \in [h; h+1[$, where $\varphi_C(\tau)$ is constant. Using (22), (24), and (32), we have

$$\begin{aligned} E_g(h, \tau_1) &= - \int_h^{\tau_1} ([\xi(h)] - [\xi(\tau)]) \dot{\xi}(\tau) d\tau \\ &= \int_h^{\tau_1} ([\xi(\tau) - \xi(h)] + [\rho(h) - \rho(\tau)]) \dot{\xi}(\tau) d\tau \\ &= E_{gz}(h, \tau_1) + E_{gq}(h, \tau_1). \end{aligned} \quad (42)$$

E_{gz} and E_{gq} are the contributions given by discretization and by the combined effect of quantization and discretization, respectively. Note that for notational simplicity, $\rho(\tau)$ stands for $\rho(\xi(\tau))$. If the device moves ($\xi(\tau_1) \neq \xi(h)$), the ZOH always injects energy into the system

$$\begin{aligned} E_{gz}(h, \tau_1) &= \int_h^{\tau_1} [\xi(\tau) - \xi(h)] \dot{\xi}(\tau) d\tau \\ &= \frac{1}{2}(\xi(\tau_1) - \xi(h))^2. \end{aligned} \quad (43)$$

The quantization error ρ is a purely positional function, without explicit time dependence. From (32), we see

$$E_{gq}(h, \tau_1) = \left(\rho(h) - \frac{1}{2} \right) ([\xi(\tau_1)] - [\xi(h)]) - \frac{1}{2}(\rho(\tau_1) - \rho(h))^2 \quad (44)$$

which, according to previous discussion, can be either positive or negative. Since ρ and $[\xi]$ are independent quantities, it is possible to maximize E_{gq} with respect to $\rho(h)$ and $\rho(\tau_1)$

$$E_{gq}(h, \tau_1) \leq \frac{1}{2} |[\xi(\tau_1)] - [\xi(h)]|. \quad (45)$$

This maximum is reached, depending whether the measured displacement $[\xi(\tau_1)] - [\xi(h)]$ is positive or negative, when $\rho(h) = \rho(\tau_1) = 0$ or $\rho(h) = \rho(\tau_1) = 1$. It is immediate to verify that in both cases, (45) simplifies to

$$E_{gq}(h, \tau_1) \leq \frac{1}{2} |\xi(\tau_1) - \xi(h)|. \quad (46)$$

The energy generated during the motion from $\xi(h)$ to $\xi(\tau_1)$ is finally at most

$$E_g(h, \tau_1) \leq \frac{1}{2}(\xi(\tau_1) - \xi(h))^2 + \frac{1}{2} |\xi(\tau_1) - \xi(h)|. \quad (47)$$

By comparing this upper bound with the lower bound (40) for the energy dissipation evaluated for $\tau_0 = h$, we can state that the dissipation inequality (30) holds if

$$\begin{aligned} &\beta \frac{(\xi(\tau_1) - \xi(h))^2}{\tau_1 - h} + \sigma |\xi(\tau_1) - \xi(h)| \\ &\geq \frac{1}{2}(\xi(\tau_1) - \xi(h))^2 + \frac{1}{2} |\xi(\tau_1) - \xi(h)| \end{aligned} \quad (48)$$

for every $\tau_1 \in [h; h+1[$ and for every $h \in \mathbb{N}$. In the event that $\xi(\tau_1) = \xi(h)$, (48) is trivially satisfied as an equality. In other cases, we can divide by $|\xi(\tau_1) - \xi(h)|$. Moreover, since the velocity is a continuous function, the mean value theorem holds

$$|\xi(\tau_1) - \xi(h)| = (\tau_1 - h) |\dot{\xi}(\tau)| \quad \tau \in [h; \tau_1[\quad (49)$$

and (48) can be rewritten as

$$|\dot{\xi}(\tau)| \left(\beta - \frac{\tau_1 - h}{2} \right) + \left(\sigma - \frac{1}{2} \right) \geq 0. \quad (50)$$

Finally, we note that $(\tau_1 - h) \in [0; 1[$ and obtain

$$|\dot{\xi}(\tau)| \left(\beta - \frac{1}{2} \right) + \left(\sigma - \frac{1}{2} \right) \geq 0 \quad \forall \tau \in \mathbb{R}. \quad (51)$$

On the (β, σ) plane, the region for which energy dissipation is guaranteed to exceed generation is then bounded by a line that rotates with slope $-|\dot{\xi}(\tau)|$ about the point $(1/2, 1/2)$. It is vertical when $|\dot{\xi}(\tau)| \rightarrow \infty$, while it is horizontal when $|\dot{\xi}(\tau)| = 0$. Therefore, the device operating point (β, σ) is guaranteed to be energy-decreasing if it belongs to region A or region E, being above the critical line characterized by the slope ξ_{\max} . In these regions, the total energy \mathcal{H}_T is a Lyapunov function.

Section III-B discusses the resulting regions in the parameter space. Here we simply note that the viscosity β provides dissipation proportional to the square of the velocity, canceling generation due to discretization. This effect is most relevant at high speeds. At lower speeds, Coulomb friction σ dominates, with dissipation proportional to velocity, and cancels generation due to quantization. Of course, the two effects may assist each other. For speeds below the maximum velocity $\dot{\xi}_{\max}$ (15), Coulomb dissipation can help viscosity to dissipate the energy due to time discretization. For regions C and D, the energy balance allows only to conclude that there exists a system trajectory for which energy can be generated at any time. The worst-case approach does not provide a formal instability condition. In region B, energy may be generated for small velocities, but is dissipated for faster motions, thus preventing diverging behaviors. Again, the worst-case approach can not provide formal conditions, but the describing function method in Section VII confirms the existence of persisting oscillations.

D. Energy Generation and Balance for $\tau_D > 0$

In the case of delayed force feedback, additional effects must be considered in the computation of energy generation. First, we note the convenient integration extrema τ_0 and τ_1 are

$$\tau_0 = l := h + \tau_D \quad \tau_1 \in [l; l+1[\quad (52)$$

In this interval, the actuated force is constant: $\varphi_A(\tau) = -[\xi(h)] - 1/2$. Therefore, by splitting the contributions of time discretization and quantization, we have

$$\begin{aligned} E_{gz}(l, \tau_1) &= \int_l^{\tau_1} [\xi(\tau) - \xi(h)] \dot{\xi}(\tau) d\tau \\ &= \frac{1}{2} (\xi(\tau_1) - \xi(l))^2 + (\xi(l) - \xi(h))(\xi(\tau_1) - \xi(l)) \end{aligned} \quad (53)$$

$$\begin{aligned} E_{gq}(l, \tau_1) &= \int_l^{\tau_1} [\rho(h) - \rho(\tau)] \dot{\xi}(\tau) d\tau \\ &= \left(\rho(h) - \frac{1}{2} \right) ([\xi(\tau_1)] - [\xi(l)]) \\ &\quad - \frac{1}{2} (\rho(\tau_1) - \rho(l))^2 + (\rho(l) - \rho(h))(\rho(\tau_1) - \rho(l)) \end{aligned} \quad (54)$$

where the last term of each expression represents the additional contribution due to time delay. For E_{gz} , it is straightforward to obtain the upper bound

$$E_{gz}(l, \tau_1) \leq \frac{1}{2} (\xi(\tau_1) - \xi(l))^2 + |\xi(l) - \xi(h)| |\xi(\tau_1) - \xi(l)| \quad (55)$$

while the maximization of (54) with respect to $\rho(h)$, $\rho(l)$, and $\rho(\tau_1)$ leads again to

$$E_{gq}(l, \tau_1) \leq \frac{1}{2} |\xi(\tau_1) - \xi(l)|. \quad (56)$$

Moreover, the mean value theorem can be applied also to

$$|\xi(l) - \xi(h)| = \tau_D |\dot{\xi}(\eta)| \quad \eta \in [h; l] \quad (57)$$

and the energy generated in the delayed case is thus bounded by

$$\begin{aligned} E_g(l, \tau_1) &\leq \frac{1}{2} (\xi(\tau_1) - \xi(l))^2 \\ &\quad + \left(\frac{1}{2} + \tau_D |\dot{\xi}(\eta)| \right) |\xi(\tau_1) - \xi(l)|. \end{aligned} \quad (58)$$

An expression analogous to (51) is finally obtained by comparing the energy dissipation evaluated in the time interval (52) and by using (49)

$$|\dot{\xi}(\tau)| \left(\beta - \frac{1}{2} - \tau_D \right) + \left(\sigma - \frac{1}{2} - \tau_D (|\dot{\xi}(\eta)| - |\dot{\xi}(\tau)|) \right) \geq 0. \quad (59)$$

If, according to (20), a maximum velocity and acceleration exist, by using $\tau - \eta \leq 1 + \tau_D$, we have

$$|\dot{\xi}(\eta)| - |\dot{\xi}(\tau)| \leq \ddot{\xi}_{\max}(\tau - \eta) \leq \ddot{\xi}_{\max}(1 + \tau_D) \quad (60)$$

which, recalling (13), leads to the expanded criterion

$$\dot{\xi}_{\max} \left(\beta - \frac{1}{2} - \tau_D \right) + \left(\sigma - \frac{1}{2} - \ddot{\xi}_{\max}(\tau_D^2 + \tau_D) \right) \geq 0. \quad (61)$$

We see that τ_D introduces additional phase lag that counters viscous dissipation. Furthermore, the delayed application of the quantized control force requires additional Coulomb friction to prevent sudden acceleration at low velocity.

VII. DESCRIBING FUNCTION ANALYSIS

The energy analysis outlined in Section VI allowed us to find a worst-case condition to ensure that energy generation due to the digital nature of the virtual wall is always dominated by the intrinsic dissipation of the device.

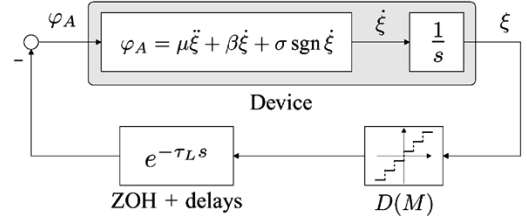


Fig. 10. Block scheme considered in the approximate describing function analysis. ZOH and other time delays are lumped together.

In contrast, describing functions [22] provide a simple and powerful tool to analyze the system behavior in the “average” case, and provide estimates of the amplitude and frequency of the self-sustained oscillations (limit cycles) predicted in Fig. 3. Moreover, since we can examine the stability of these oscillations as well, it is possible to use it to estimate the boundary on the (β, σ) parameter plane between unstable and stable behaviors.

In the following, we will refer to the simplified diagram description Fig. 10, where the dimensionless formulation (7) is used. In particular, the ZOH is approximated by a time delay of $1/2$ and then lumped with τ_D . The encoder is represented by its describing function $D(M)$. Note that because of the integration required to obtain the position ξ from the velocity $\dot{\xi}$, the loop transfer function has a low-pass characteristic that justifies the first-order approximation involved in the application of the describing function method.

Let $\tau_L = 1/2 + \tau_D$ be the total loop time delay. $G(M, \omega)$ approximates the nonlinear mapping from φ_A to ξ , representing the haptic device. From the Nyquist criterion, self-sustained oscillations are likely to arise if

$$G(M, \omega) e^{-j\tau_L \omega} = -\frac{1}{D(M)}. \quad (62)$$

A. Describing Function of the Device Model

If we suppose the existence of a sinusoidal motion of amplitude M (measured in encoder ticks)

$$\xi(\tau) = M \sin(\omega \tau) \quad M > 0, \quad \omega > 0 \quad (63)$$

then the required actuation force is

$$\varphi_A(\tau) = -\mu M \omega^2 \sin(\omega \tau) + \beta M \omega \cos(\omega \tau) + \sigma \operatorname{sgn}(M \omega \cos(\omega \tau)). \quad (64)$$

Assuming that φ_A is also sinusoidal and neglecting higher order harmonics [22], we approximate the sign function to obtain

$$\varphi_A(\tau) = -\mu M \omega^2 \sin(\omega \tau) + \left[\beta \omega + 4 \frac{\sigma}{\pi M} \right] M \cos(\omega \tau). \quad (65)$$

Therefore, the device is described by

$$\begin{aligned} G(M, \omega) &= \frac{\Xi(M, \omega)}{\Phi_A(M, \omega)} \\ &= \frac{1}{-\mu \omega^2 + j \left(\beta \omega + 4 \frac{\sigma}{\pi M} \right)} \end{aligned} \quad (66)$$

where $\Phi_A(M, \omega)$ and $\Xi(M, \omega)$ are the Fourier transforms of $\varphi_A(\tau)$ and $\xi(\tau)$. The dependency on the amplitude M is required to capture the nonlinear effect of Coulomb friction.

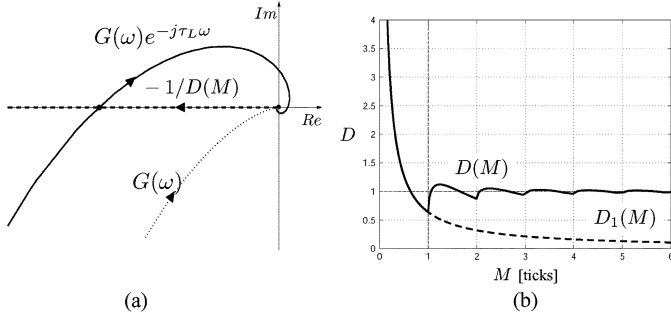


Fig. 11. (a) Nyquist plots without Coulomb friction show the existence of limit cycles at finite frequency for $\tau_L > 0$. (b) Encoder describing function $D(M)$ (solid) matches, for $M < 1$, its first term $D_1(M)$ (dash).

B. Describing Function of the Quantization

Since the quantization nonlinearity (22) is static and odd with respect to ξ , $D(M)$ is real and does not depend on the frequency ω . Under the hypothesis (63), the quantization block is approximated by the expression

$$D(M) = \frac{2}{\pi M} + \frac{4}{\pi M^2} \sum_{l=1}^{\lfloor M \rfloor} \sqrt{M^2 - l^2}. \quad (67)$$

If, for the moment, we assume no Coulomb friction, the Nyquist plots in Fig. 11(a) graph condition (62) without and with delay. For $\tau_L = 0$, the condition is satisfied and oscillations can only occur at infinite frequency with zero amplitude. With a ZOH or other delays ($\tau_L > 0$), the curves intersect at finite frequency and amplitude. This confirms that limit cycles arise because of quantization nonlinearity, even without Coulomb friction.

In Fig. 11(b), we see that $D(M)$ matches its first term $D_1(M) = 2/(\pi M)$ for small amplitudes. As M exceeds unity, $D(M)$ quickly tends to unity. In other words, the quantization effects are most relevant for small motions, while the quantized measurements are good approximations of the real displacements for $M > 1$. Within the limits of the approximate quasi-linear analysis, (62) can be solved in these two separate cases, leading to two different families of oscillations.

C. Solution for Small Amplitude ($M < 1$)

If we assume $D(M) \simeq D_1(M)$, the condition (62) for the existence of a limit cycle can be rearranged into

$$\begin{cases} \frac{2}{\pi M} \cos(\tau_L \omega) = \mu \omega^2 \\ \frac{2}{\pi M} \sin(\tau_L \omega) = \beta \omega + \frac{4\sigma}{\pi M} \end{cases} \quad (68)$$

From the first equation, we relate frequency to magnitude via

$$M = \frac{2}{\pi \mu} \frac{\cos(\tau_L \omega)}{\omega^2} \quad (69)$$

This admits exactly one solution for $\omega < \pi/(2\tau_L)$, and states that the amplitude decreases for larger values of the dimensionless inertia μ . Since analytic determination of the frequency ω is difficult from (68), it is more convenient to identify the (β, σ)

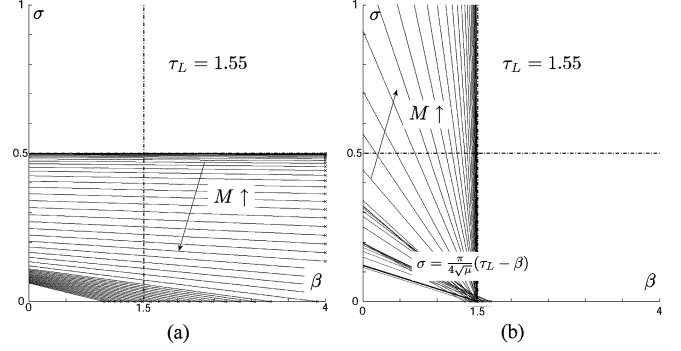


Fig. 12. Contour maps of amplitude and frequency of small (left) and large (right) oscillations on the (β, σ) plane for $\mu = 5$. (a) $M < 1$: stable oscillations. (b) $M > 1$: unstable oscillations.

parameters necessary to achieve a given ω . By combining (68) with (69), we find

$$\sigma = \frac{1}{2} \sin(\tau_L \omega) - \frac{\beta}{2\mu\omega} \cos(\tau_L \omega) \quad \omega \in \left[0; \frac{\pi}{2\tau_L}\right]. \quad (70)$$

This describes a line on the (β, σ) plane. Fig. 12(a) shows the set of lines obtained for different values of amplitude and frequency, clearly supporting the fact that small amplitude oscillations can occur only if $\sigma < 1/2$. With increasing amplitude M , σ and ω decrease from $1/2$ and $\pi/(2\tau_L)$, respectively. Finally, the stability analysis of the Nyquist plot shows that these limit cycles are stable. This type of oscillation was detected in Fig. 8(b) with an amplitude bounded by one encoder tick.

D. Solution for Large Amplitude ($M > 1$)

For large amplitudes, the encoder describing function approximates $D(M) \simeq 1$ and (67) reduces to the classic Nyquist criterion. These limit cycles are unstable, i.e., oscillations above a critical value grow unbounded, while smaller oscillations decay. As such, the solutions to (67) determine a stability boundary. In particular, we have

$$\begin{cases} \cos(\tau_L \omega) = \mu \omega^2 \\ \sin(\tau_L \omega) = \beta \omega + \frac{4\sigma}{\pi M} \end{cases} \quad (71)$$

The first equation forces a solution for $\omega < \frac{\pi}{2\tau_L}$ independent of M , while the second leads to

$$\sigma = \frac{\pi M}{4} (\sin(\tau_L \omega) - \beta \omega) \quad \omega \in \left[0; \frac{\pi}{2\tau_L}\right]. \quad (72)$$

Positive values of σ require $\beta \leq \tau_L$ and, as Fig. 12(b) shows, the solutions occur only in regions of small viscous friction. Moreover, if the frequency is sufficiently small to approximate $\cos(\tau_L \omega)$ and $\sin(\tau_L \omega)$ by their series expansions, we have

$$\omega \simeq \frac{1}{\sqrt{\mu + \frac{1}{2}\tau_L^2}} \quad (73)$$

and (72) becomes

$$\sigma = \frac{\pi}{4} M \omega (\tau_L - \beta). \quad (74)$$

The substitution $\dot{\xi}_{\max} = M\omega$, corresponding to the maximum velocity for sinusoidal oscillations, highlights the similarity to

the critical line separating the stable and unstable regions D and E in Figs. 3 and 5. With respect to the energetic analysis, (72) intersects the point $(1/2 + \tau_D, 0)$ instead of $(1/2 + \tau_D, 1/2)$. This is consistent with the fact that (19) is obtained through a worst-case analysis, while (75) describes the “average” behavior.

Finally, we note that if $\mu \gg \tau_L^2/2$ and with $M > 1$, the system can be stable only if

$$\sigma \geq \frac{\pi}{4\sqrt{\mu}}(\tau_L - \beta). \quad (75)$$

Below this line, the Nyquist criterion confirms, within the limits of this approximate analysis, that the system is unstable.

VIII. CONCLUSION

This paper has examined the stability of a haptic display. It relates the inertia, viscous, and Coulomb friction of the device to the controller stiffness, sampling rate, encoder resolution, and computational or amplifier delay. The dimensionless approach highlights critical parameters and identifies distinct stability regions.

The nonlinear effects of quantization and Coulomb friction lead to multiple behaviors categorized as passive, locally stable, limit cycles, and unstable. Of particular importance is the condition of stability that occurs for devices with limited viscous damping. Most current devices fall in this category and violate traditional passivity conditions. But both a worst-case and an average-case analysis shows why Coulomb friction allows them to operate successfully.

We hope this paper will provide better insights on what performance level can be expected from existing haptic systems and how to best trade off system parameters. We also hope to inspire better controllers and ultimately improve the design of future haptic systems.

REFERENCES

- [1] N. Diolaiti, G. Niemeyer, F. Barbagli, and J. Salisbury, “A passivity criterion for haptic devices,” in *Proc. IEEE Int. Conf. Robot. Autom.*, Barcelona, Spain, Apr. 2005, pp. 2463–2468.
- [2] N. Diolaiti, G. Niemeyer, F. Barbagli, J. K. Salisbury, and C. Melchiorri, “The effect of quantization and Coulomb friction on the stability of haptic rendering,” in *Proc. 1st World Haptics Conf.*, Pisa, Italy, Mar. 2005, pp. 237–246.
- [3] T. Yoshikawa, Y. Yokokohji, T. Matsumoto, and X. Zheng, “Display of feel for the manipulation of dynamic virtual objects,” *ASME J. Dyn. Syst., Meas., Control*, vol. 117, no. 4, pp. 554–558, 1995.
- [4] T. Massie and J. Salisbury, “The phantom haptic interface: A device for probing virtual objects,” in *Proc. ASME Winter Annu. Meeting*, vol. 55-1, New Orleans, LA, 1994, pp. 295–300.
- [5] F. Barbagli and J. Salisbury, “The effect of sensor/actuator asymmetries in haptic interfaces,” in *Proc. IEEE Haptics Symp.*, Los Angeles, CA, Mar. 2003, pp. 140–147.
- [6] J. Colgate, P. Grafing, M. Stanley, and G. Schenkel, “Implementation of stiff virtual walls in force-reflecting interfaces,” in *Proc. IEEE Virtual Reality Symp.*, 1993, pp. 202–208.
- [7] J. Colgate and G. Schenkel, “Passivity of a class of sampled-data systems: Application to haptic interfaces,” in *Proc. Amer. Control Conf.*, Baltimore, MD, Jun. 1994, pp. 3236–3240.
- [8] B. Gillespie and M. Cutkosky, “Stable user-specific rendering of the virtual wall,” in *Proc. ASME IMECE*, vol. DSC-vol. 58, Atlanta, GA, Nov. 1996, pp. 397–406.

- [9] N. Hogan, “Controlling impedance at the man/machine interface,” in *Proc. IEEE Int. Conf. Robot. Autom.*, 1989, pp. 1626–1631.
- [10] R. Ellis, N. Sarkar, and M. Jenkins, “Numerical methods for the force reflection of contact,” *ASME J. Dyn. Syst., Meas., Control*, vol. 119, pp. 768–774, 1997.
- [11] B. Hannaford and J. Ryu, “Time-domain passivity control of haptic interfaces,” in *Proc. IEEE Int. Conf. Robot. Autom.*, Seoul, Korea, May 2001, pp. 1863–1869.
- [12] S. Stramigioli, C. Secchi, A. van der Schaft, and C. Fantuzzi, “A novel theory for sample data system passivity,” in *Proc. IEEE/RSJ Int. Conf. Intell. Robots Syst.*, vol. 2, Lausanne, Switzerland, Oct. 2002, pp. 1936–1941.
- [13] B. Miller, J. Colgate, and R. Freeman, “On the role of dissipation in haptic systems,” *IEEE Trans. Robot.*, vol. 20, no. 4, pp. 768–771, Aug. 2004.
- [14] M. Mahvash and V. Hayward, “High-fidelity passive force reflecting virtual environments,” *IEEE Trans. Robot.*, vol. 21, no. 1, pp. 38–46, Feb. 2005.
- [15] J. J. Abbott and A. M. Okamura, “Effects of position quantization and sampling rate on virtual-wall passivity,” *IEEE Trans. Robot.*, vol. 21, no. 5, pp. 952–964, Oct. 2005.
- [16] W. Townsend and J. Salisbury, “The effect of Coulomb friction and stiction on force control,” in *Proc. IEEE Int. Conf. Robot. Autom.*, 1987, pp. 883–889.
- [17] A. van der Schaft, *L2-Gain and Passivity Techniques in Nonlinear Control*, ser. Communication and Control Engineering. New York: Springer-Verlag, 2000.
- [18] J. Willems, “Dissipative dynamical systems, Part I: General theory,” *Arch. Rat. Mech. Ann.*, vol. 45, pp. 321–351, 1972.
- [19] C. Zilles, “Haptic rendering with the Toolhandle haptic interface,” Master’s thesis, Mass. Inst. Technol., Cambridge, MA, 1995.
- [20] K. Kuchenbecker and G. Niemeyer, “Modeling induced master motion in force-reflecting teleoperation,” in *Proc. IEEE Int. Conf. Robot. Autom.*, Barcelona, Spain, Apr. 2005, pp. 348–353.
- [21] K. Kuchenbecker, J. Park, and G. Niemeyer, “Characterizing the human wrist for improved haptic interaction,” in *Proc. ASME Int. Mech. Eng. Congr. Expo.*, vol. 2, Washington, DC, Nov. 16–21, 2003, Paper #42017.
- [22] J. Slotine and W. Li, *Applied Nonlinear Control*. Englewood Cliffs, NJ: Prentice-Hall, 1991.



Nicola Diolaiti (S’02) received the M.Sc. degree (*cum laude*) in electrical engineering in July 2001, and the Ph.D. degree in automatic control and operational research in March 2005, both from the University of Bologna, Bologna, Italy.

In 2003, he visited the Drebhel Institute, University of Twente, Enschede, The Netherlands, and in 2004 and 2005, he was appointed Visiting Scholar at the Stanford AI-Robotics Lab, Stanford University, Stanford, CA. His research activity is focused on the modeling and control aspects of interactive robotic

systems, and in particular, on bilateral teleoperation and haptic interfaces.



Günter Niemeyer (M’02) received the M.S. and Ph.D. degrees from the Massachusetts Institute of Technology (MIT), Cambridge, in the areas of adaptive robot control and bilateral teleoperation, introducing the concept of wave variables.

Currently, he is an Assistant Professor in Mechanical Engineering at Stanford University, Stanford, CA, and directs the Telerobotics Lab. His research examines human–robotic interactions, force sensitivity and display, and teleoperation. Medical devices, in particular, telesurgery, form a primary application. His work also addresses haptic feedback and the effects of delayed or network transmissions on user perception, both in training, simulation, and operation. Previously, he held a postdoctoral research position at MIT developing surgical robotics. In 1997, he joined Intuitive Surgical Inc., Sunnyvale, CA, where he helped create the daVinci minimally invasive surgical system. He joined the Stanford faculty in the fall of 2001.



Federico Barbagli (M'01) received the Master's degree in computer science from the University of Bologna, Bologna, Italy, in 1998, and the Ph.D. degree in robotics from Scuola Superiore S. Anna, Pisa, Italy, in 2002.

In 2001 and 2002, he was a Visiting Researcher at the Stanford Robotics Lab, Stanford University, Stanford, CA. Between 2002 and 2004, he was an Assistant Professor at the University of Siena, Siena, Italy, and a Post Doctoral Fellow at Stanford University. In 2004, he joined Hansen Medical, a medical robotics startup, as a Senior Haptics and Visualization Engineer, while still collaborating with the Stanford Robotics Lab as a Research Fellow. He is one of the founding members and architects of the *chai3d* project.



J. Kenneth Salisbury, Jr. received the Ph.D. degree in mechanical engineering from Stanford University, Stanford, CA.

He is currently a member of the faculty at Stanford University, with the departments of Computer Science and Surgery. His research interests include robotics, haptics, human-machine interaction, collaborative computer-mediated haptics, and surgical simulation. Among the projects with which he has been associated are the Stanford-JPL Robot Hand, the JPL Force-Reflecting Hand Controller, the MIT Whole Arm Manipulator, and the Black Falcon Surgical Robot. His work with haptic interface technology led to the founding of SensAble Technologies, producers of the Phantom haptic interface and FreeForm software. He was a Scientific Adviser to Intuitive Surgical, where his efforts focused on the developing dexterity-enhancing telerobotic systems for surgeons. He has served on the National Science Foundation's Advisory Council for Robotics and Human Augmentation, and as Technical Adviser to Robotic Ventures.